





Article

Immobilized Nano-TiO₂ Photocatalysts for the Degradation of Three Organic Dyes in Single and Multi-Dye Solutions

Umberto Bellè ¹, Filippo Pelizzari ¹, Andrea Lucotti ², Chiara Castiglioni ²,
Marco Ormellese ¹, MariaPia Pedferri ¹ and Maria Vittoria Diamanti ^{1,*}

¹ Department of Chemistry, Materials and Chemical Engineering “G. Natta”, Politecnico di Milano, Via Mancinelli 7, 20131 Milan, Italy; umberto.belle@polimi.it (U.B.); filippo.pelizzari@mail.polimi.it (F.P.); marco.ormellese@polimi.it (M.O.); mariapia.pedferri@polimi.it (M.P.)

² Department of Chemistry, Materials and Chemical Engineering “G. Natta”, Politecnico di Milano, Piazza Leonardo da Vinci 32, 20133 Milan, Italy; andrea.lucotti@polimi.it (A.L.); chiara.castiglioni@polimi.it (C.C.)

* Correspondence: mariavittoria.diamanti@polimi.it; Tel.: +39-02-2399-3137

Received: 3 September 2020; Accepted: 22 September 2020; Published: 25 September 2020



Abstract: Heterogeneous photocatalysis with titanium dioxide (TiO₂) is considered one of the most promising Advanced Oxidation Processes (AOPs). In order to solve issues related to catalyst recovery and possible agglomeration, which are typical of catalysts in nanoparticle form, self-organized nanotubular TiO₂ films directly immobilized on a metal substrate can be produced through anodization. In this study, a nanotubular anodic oxide was tested in the degradation of three organic dyes, namely Direct Red 80, Methylene Blue, and Rhodamine B, in single, binary, and ternary mixtures, to simulate industrial effluents with the co-presence of multiple dyes. To better understand the dyes' behavior and possible interaction effects, spectrophotometry was used to analyze the degradation of each dye in the mixture. The zero-crossing first-order derivative approach and double divisor ratio spectra derivative method were used for the analysis of binary and ternary mixtures, respectively, to overcome quantification problems due to spectra overlapping. The photocatalytic system demonstrated good efficiency, supporting the use of nanotubular TiO₂ as a photocatalyst for dye mixtures. Moreover, the interaction among dyes can actually affect, both positively and negatively, photodegradation kinetics, posing an issue in understanding the actual efficiency of the purification process as a function of the effluent composition.

Keywords: titanium dioxide; nanotubes; photocatalysis; dyes; derivative absorption spectrophotometry

1. Introduction

Advanced Oxidation Processes (AOPs) have demonstrated to be promising techniques for the removal of dyes from textile wastewaters; in particular, photocatalysis has been widely studied, since it can lead to a complete mineralization of organic pollutants by exploiting solar energy, making wastewater treatments more sustainable and environmentally friendly [1–3].

The use of nanostructured titanium dioxide (TiO₂) as a photocatalyst has gained particular attention due to its high stability in different pH ranges, non-toxicity, biocompatibility, environmental sustainability, and low cost; moreover, its redox properties allow reaching a high level of photodegradation efficiency by exploiting UV rays for the generation of oxidizing agents [2–7].

The necessity of improving photocatalytic efficiency has driven scientific research in the generation of nanostructured oxides for increasing the surface-to-volume ratio and so promoting interactions between photocatalyst and organic pollutants. In this sense, anodic oxidation allows forming

self-organized nanotubular TiO₂ films strongly immobilized on the substrate, facilitating the adsorption of organic pollutants on the photocatalyst surface, while enhancing light adsorption and avoiding recovery issues typical of nanoparticles. These films are achieved by imposing a cell voltage between the titanium sample (anode) and a counter electrode (cathode) in a fluoride containing organic electrolyte; this causes the growth of an amorphous oxide layer on the Ti specimen, while fluorides dissolves locally the growing oxide, hence generating a nanotubular morphology. Instead, calcination treatments promote oxide crystallization, thus improving the mobility of the photogenerated charge carriers [8–13].

Limited studies on the degradation of a multi-dye system have been performed, yet dye quantification in such systems and interactions with other dyes should be taken into account in designing photocatalytic devices. However, such tasks are complex in the presence of strong spectra overlapping, where the application of Beer–Lambert law to the dye main absorption peak is unsatisfactory due to its low accuracy quantifying dye concentrations inside mixtures [14].

Different analytical methods have proved to be successful, such as chromatographic methods [15], capillary electrophoresis [16], and multivariate calibration approaches [17–19]. Among them, derivative spectrophotometry provides a good selectivity in terms of quantitative and qualitative information by exploiting the first-order (or higher-order) derivatives of absorbance spectra; the so-obtained derivative spectra provide new well-defined peaks of large intensity, leading to a discrimination of overlapped spectra and offering the selective identification of each dye in the multi-dye mixture [20–23]. Moreover, derivative spectrophotometry is quicker and easier if compared to alternative methods since it requires neither sophisticated instrumentation nor any separation steps [24].

Different derivative approaches can be exploited depending on the evaluated system; zero-crossing first-order derivative spectrophotometry is used in the analysis of binary mixtures [20,21], whereas ternary mixtures require different derivative spectrophotometric approaches, such as double divisor ratio spectra derivative spectrophotometry, as proposed by Dinç et al. [24,25] basing on the works of Salinas and Nevado [26,27]. This technique allows analyzing and quantifying each compound in a ternary mixture having highly overlapped absorbance bands by analyzing the first derivative of the ratio among the absorbance spectra of the ternary mixture and a binary mixture one.

Despite the existence of different approaches, analysis of effects of dyes' interaction on the photodegradation kinetics in a ternary mixture has been rarely studied. For this reason, this work proposes an analysis of photocatalytic properties of nanotubular TiO₂ films for the photodegradation of multi-dye aqueous solutions, in order to understand whether dye mixing affects the photocatalytic process and therefore, in perspective, the purification of real effluents. Three different organic dyes, i.e., Direct Red 80, Methylene Blue, and Rhodamine B, were chosen. The photodegradation of binary and ternary mixtures was monitored through derivative absorbance spectrophotometry, using zero-crossing first-derivative and double-divisor ratio spectra methods, respectively, to monitor the variation of dye concentrations as an estimation of the photocatalytic efficiency.

2. Models Adopted

In this work, we propose two different methods for analyzing in a simple and accurate way the composition of binary and ternary mixtures, i.e., zero-crossing first-derivative spectrophotometry and double divisor ratio spectra derivative spectrophotometry. Instead, the concentration of dyes in single-dye solutions was examined through the zero-order spectrophotometric approach based on Beer–Lambert law, which is typically adopted in the literature for dye degradation analyses [11,28,29].

For the development of the model used for binary mixtures, the Beer–Lambert law must be recalled [20,22]; according to this, the absorbance value of an X component at wavelength λ_i is:

$$A_{X,\lambda_i} = \varepsilon_{X,\lambda_i} C_X \quad (1)$$

where A_{X,λ_i} is the absorbance of the compound X , recorded at a certain wavelength λ_i , while $\varepsilon_{X,\lambda_i}$ defines the absorptivity of the component having concentration C_X (the optical path length l , being constant, is here considered in the terms $\varepsilon_{X,\lambda_i}$ and $\varepsilon_{Y,\lambda_i}$).

In a binary mixture containing the X and Y components, the absorbance value at a certain wavelength, λ_i , can be expressed as:

$$A_{m,\lambda_i} = \varepsilon_{X,\lambda_i} C_X + \varepsilon_{Y,\lambda_i} C_Y. \quad (2)$$

Equation (2) holds in the hypothesis that the absorption spectrum of the mixture merely corresponds to the superposition of the contributions from the two species, namely in the hypothesis of weakly interacting X and Y components.

By deriving the ratio between Equation (2) and the absorbance of X given by Equation (1) vs. λ , Equation (2) becomes:

$$\frac{d}{d\lambda} \left[\frac{A_{m,\lambda}}{\varepsilon_{X,\lambda} C_X} \right]_{\lambda_i} = \frac{d}{d\lambda} \left[\frac{\varepsilon_{Y,\lambda}}{\varepsilon_{X,\lambda} C_X} \right]_{\lambda_i} C_Y + \frac{d}{d\lambda} [1]_{\lambda_i} \quad (3)$$

where the last term is null, being the derivative of a constant value.

It can be demonstrated that in correspondence to certain wavelength values λ_i , in which the derivative absorbance of the X component is zero, while the derivatives of both the Y component and the binary solution have non-zero values, it is possible to analyze the contribution of the Y component and so to draw calibration curves by representing the $\frac{d}{d\lambda} \left[\frac{A_{m,\lambda}}{\varepsilon_{X,\lambda} C_X} \right]_{\lambda_i}$ function of only C_Y , thus complying with Beer–Lambert law. In an analogous way, it is possible to evaluate C_X in its binary mixture with Y .

Regarding double divisor ratio spectra derivative spectrophotometry, the approach is similar to the previous one [24,25]; considering a system containing three different compounds (X , Y and Z), the absorption value at wavelength λ_i is so defined:

$$A_{m,\lambda_i} = \varepsilon_{X,\lambda_i} C_X + \varepsilon_{Y,\lambda_i} C_Y + \varepsilon_{Z,\lambda_i} C_Z. \quad (4)$$

A standard solution of two of the three dyes, for instance X and Y , is defined and named double divisor, where the concentrations of the double divisor C_X^0 and C_Y^0 must be equal [26]. Then, the absorption spectrum of the double divisor is represented by:

$$A_{m,\lambda_i}^0 = \varepsilon_{X,\lambda_i} C_X^0 + \varepsilon_{Y,\lambda_i} C_Y^0 = C_X^0 [\varepsilon_{X,\lambda_i} + \varepsilon_{Y,\lambda_i}]. \quad (5)$$

If the absorbance of the ternary mixture is divided by the standard double divisor (Equation (5)), then the resulting ratio spectrum is derived with respect to λ , and Equation (4) becomes:

$$\frac{d}{d\lambda} \left[\frac{A_{m,\lambda}}{C_X^0 [\varepsilon_{X,\lambda} + \varepsilon_{Y,\lambda}]} \right]_{\lambda_i} = \frac{d}{d\lambda} \left[\frac{\varepsilon_{Z,\lambda}}{\varepsilon_{X,\lambda} + \varepsilon_{Y,\lambda}} \right]_{\lambda_i} \frac{C_Z}{C_X^0} + \frac{d}{d\lambda} \left[\frac{\alpha_{X,\lambda} C_X + \beta_{Y,\lambda} C_Y}{C_X^0 (\alpha_{X,\lambda} + \beta_{Y,\lambda})} \right]_{\lambda_i} \quad (6)$$

where the last term is null, since the ratio is constant with respect to λ_i [25].

Equation (6) shows that the derivative signal of the ternary mixture depends only on the concentration C_Z and on the chosen concentration of the double divisor, $C_X^0 = C_Y^0$, which is constant, whereas it is independent of the concentration C_X and C_Y . Hence, this approach allows drawing the calibration curve of Z in an $X + Y + Z$ system in correspondence of wavelength values where the coincident points reach their maximum (or minimum). Coincident points are those in which the absorbance derivative of pure Z and the one of Z in the ternary mixture with X and Y have the same value [24,25]. In the same way, it is possible to determine the contribution of both X and Y in the $X + Y + Z$ ternary mixture.

For both derivative approaches, it may be possible to identify more than an adequate wavelength; in this situation, the most correct value is taken in correspondence to the one in which the value of $dA/d\lambda$ is higher in absolute value.

These methods require not only a calibration step but also an estimation step for evaluating the accuracy of the exploited approaches. The accuracy was tested by calculating recoveries (%) and errors (%), according to the following equations:

$$\text{Recovery (\%)} = \frac{C_m}{C_t} \times 100 \quad (7)$$

$$\text{Error (\%)} = \frac{C_m - C_t}{C_t} \times 100 \quad (8)$$

where C_t is the theoretical concentration of the compound, i.e., the concentration of the solution obtained by diluting the stock solutions, and C_m is the concentration measured through absorbance measurements and the subsequent use of calibration curves.

3. Materials and Methods

3.1. Quantification of Dyes in Single, Binary, and Ternary Mixtures

Direct Red 80 (DR80; $C_{45}H_{26}N_{10}Na_6O_{21}S_6$, $MM = 1373.07 \text{ g}\cdot\text{mol}^{-1}$), Methylene Blue (MB; $C_{16}H_{18}ClN_3S$, $MM = 319.85 \text{ g}\cdot\text{mol}^{-1}$) and Rhodamine B (RhB; $C_{28}H_{31}ClN_2O_3$, $MM = 479.01 \text{ g}\cdot\text{mol}^{-1}$) are the dyes evaluated in this study and they were supplied by Sigma-Aldrich. These dyes are soluble in water and they do not require any pre-treatment before their usage. The chemical structures together with the absorbance spectra of equimolar single-dye solutions (10^{-5} M) in the visible range are shown in Figure 1; this figure points out that these dyes have similar absorptivity ($\ln \epsilon$, evaluated at the maximum peak for each dye by simply dividing the absorbance with respect to the dye concentration, is equal to 11.4, 11.05, and 11.54 for DR80, MB, and RhB, respectively).

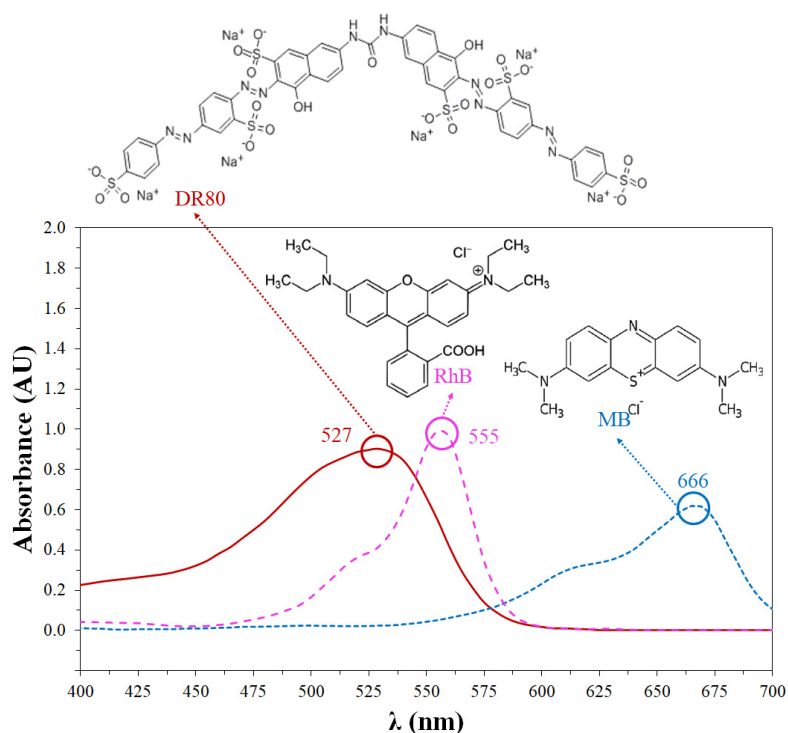


Figure 1. Absorbance spectra of aqueous single-dye solutions (10^{-5} M) in the visible range.

The stock solutions of DR80, MB, and RhB (3×10^{-3} M) were prepared by dissolving the dye in distilled water; their pH was measured with litmus papers, verifying that it was equal to the distilled water one (pH 6) for all of them. Single-dye, binary, and ternary mixtures were prepared by diluting the stock solutions and by mixing them (DR80 + MB, DR80 + RhB, MB + RhB, and DR80 + MB + RhB) at different dye concentrations; the solutions used for the building up of the calibration curves in the evaluated mixtures are reported in Tables S1–S3.

The absorbances of all the studied solutions were measured in the visible light range with a spectrophotometer SPECTRONIC 200E (Thermo Fisher Scientific, Les Ulis, France), and all the spectra were recorded using identical polystyrene cuvettes and instrument geometry, so that the optical path length l is considered constant.

For single-dye solutions, the measurements were performed according to zero-order spectrophotometry by simply applying the Beer–Lambert law at the maximum absorbance peak, 527, 555, and 666 nm for DR80, MB, and RhB, respectively (Figure 1). Calibration curves (absorbance versus dye concentration) were calculated using 5 points for each dye (Table S1).

For $X + Y$ binary systems, the analyses were performed with the zero-crossing first-order derivative approach; for each binary solution, a first set of experiments was conducted maintaining constant C_X for drawing up the calibration curve for Y through the variation of its concentration; vice versa, a second set of experiments was performed, varying the concentration of X , at constant C_Y .

The method was applied in correspondence of zero-crossing points, as explained in the previous paragraph. Derivative spectra were obtained by calculating according to Equation (9):

$$\left[\frac{dA_{\text{bin}}}{d\lambda} \right]_{\bar{\lambda}} = \frac{A_{\text{bin}}(\bar{\lambda} + \Delta\lambda) - A_{\text{bin}}(\bar{\lambda})}{\Delta\lambda} \quad (9)$$

where A_{bin} is the absorption spectrum of the binary mixture and $\bar{\lambda}$ refers to the wavelength belonging to the visible range (400–700 nm), at which the derivative is evaluated.

According to Equation (9), the derivative is calculated numerically adopting a suitable increment $\Delta\lambda$. The literature reports a spread range of $\Delta\lambda$ values, ranging between 4 and 10 nm [24–27,30,31], since it must be chosen based on the sensitivity of the used experimental apparatus; in this work, preliminary tests with two different $\Delta\lambda$ values, namely 5 and 10 nm, were performed in order to choose the proper one. Data obtained in both cases were very similar; hence, the 5 nm value was chosen to better approximate the definition of an incremental limit ratio, still respecting the effective accuracy of the used experimental apparatus for collecting data.

Ternary mixtures were analyzed through the double divisor ratio spectra derivative method. For building up the calibration curves of a ternary solution containing X , Y , and Z dyes, different solutions were prepared by varying the concentration of X at fixed concentrations of Y and Z ; the collected spectra were so divided by a standard double divisor $Y^0 + Z^0$, and the derivative signals were analyzed.

This procedure was repeated for each dye.

Three standard double divisors were selected, namely $\text{DR80}^0 + \text{MB}^0$, $\text{DR80}^0 + \text{RhB}^0$, and $\text{MB}^0 + \text{RhB}^0$, whose proper concentration was evaluated in a preliminary study. An accurate choice of standard double divisor concentration is mandatory, since they can drastically influence the results [26,32]. Particularly, the resulting first-derivative signals are proportionally decreased if the concentration of the standard solution, i.e., the divisor, increases, and vice versa, even though the maxima and minima positions remain fixed at the same wavelengths; consequently, the slope of the resulting calibration curve decreases, leading to a poor data differentiation [26,27]. On the other hand, too low standard double divisor concentrations could increase the signal-to-noise ratio, affecting the ratio derivative, with a consequent increase in the standard error of the estimations [32,33]. In this study, three equimolar double divisors were chosen, so that $C_{\text{DR80}}^0 = C_{\text{MB}}^0 = C_{\text{RhB}}^0 = 2.5 \times 10^{-6}$ M; this choice represents the best balance among data differentiation, linearity range, and experimental errors generated. Again, $\Delta\lambda$ was fixed at 5 nm.

Recoveries and errors were evaluated according to Equations (7) and (8); the results are reported in the Supplementary Information.

3.2. Nanotubular TiO₂ Production and Characterization

Experimental tests were performed on $3 \times 3 \times 0.5 \text{ cm}^3$ titanium (ASTM Grade 2) sheets polished with P600 SiC paper for the removal of titanium oxide naturally grown on the sample surfaces. After 5 min of ultrasonic cleaning treatment in EtOH, each sample was anodized in ethylene glycol (EG) + 0.2 M of NH₄F + 2 M of H₂O at 45 V for 30 min in potentiostatic conditions, as reported in previous studies [14,29]. All the chemicals were purchased from Sigma-Aldrich; all the reagents were analytical grade. A titanium mesh was selected as the cathode [34]. Subsequently, samples were carefully rinsed with distilled water and subjected to annealing at 500 °C for 2 h.

Scanning Electron Microscopy (SEM) was performed with an EVO Series 50 (Carl Zeiss AG, Oberkochen, Germany), and ImageJ software (version 1.52t) was used for the analysis of SEM results. X-Ray Diffraction (XRD) was performed with an Empyrean diffractometer (Malvern Panalytical, Malvern, UK), using Cu K α and Cu K β radiations.

3.3. Photocatalytic Degradation Test

The photoactivity of TiO₂ nanotubular arrays was tested by using a batch photoreactor built during the experimental stage, consisting of a beaker containing 40 mL of the tested solution and a stirring system (in turbulent regime) to allow both the homogenization of dye concentrations in the solution and a continuous oxygen influx at the photocatalyst surface. A UV-A LED (Nichia NCSU033B, $\lambda_{\text{radiation peak}} = 365 \text{ nm}$, UV-A intensity = $11.1 \text{ mW} \cdot \text{cm}^{-2}$, Tokushima, Japan) was positioned on top, at a distance of 3 cm from the sample. A schematic representation and a photograph of the batch photoreactor are shown in Figure S1.

As previously described, photocatalytic efficiency was evaluated on the basis of dye discoloration, obtained by measuring dye absorbance in the visible light range with a spectrophotometer SPECTRONIC 200E (Thermo Fisher Scientific, Les Ulis, France). Absorbance measurements were repeated every 30 min and dye concentration was derived using the Beer–Lambert law, zero-crossing first-order derivative approach, and double divisor ratio spectra derivative method for single-dye, binary, and ternary mixtures, respectively.

Data were used for calculating the reaction rate constant k , considering a pseudo-first-order Langmuir–Hinshelwood kinetic model:

$$\ln\left(\frac{C}{C_0}\right) = -kt \quad (10)$$

where C_0 is the initial dye concentration and t is the irradiation time. Instead, photocatalytic efficiency was measured as:

$$\text{PE (\%)} = \frac{(C_0 - C_3)}{C_0} \times 100 \quad (11)$$

where C_3 is dye concentration at 3 h.

Photodegradation tests were performed in equimolar (10^{-5} M) single-dye, binary, and ternary solutions. The three single-dye aqueous solutions, having an initial concentration of 10^{-5} M and containing DR80, MB, and RhB, were firstly tested. Then, three binary mixtures, obtained by mixing all the combinations of single-dye solutions (50/50 vol.%) were analyzed, where the initial dye concentration was halved ($5 \times 10^{-6} \text{ M}$ for each dye) to obtain an overall solution molarity in the reactor equal to that of single-dye tests. The same applies to the ternary mixture, containing all single-dye solutions in the same volumetric quantity at a concentration of $3.3 \times 10^{-6} \text{ M}$ for each dye. Further tests were performed to double check the effect of dye concentration on kinetics, using single-dye solutions with a concentration of $3.3 \times 10^{-6} \text{ M}$.

Each test was performed three times to ensure good reproducibility of the results, and each sample was reused up to six times. Both reusability tests (the same sample used multiple times) and repeatability tests (the same test on different samples anodized in the same conditions) showed similar trends in the measured photoactivity: the variation observed among all tests is generally lower than 7%; hence, in the following, only larger differences in photoactivity will be considered as significant.

Adsorption tests by dark storage and photolysis tests in the absence of a photocatalyst were also performed for each analyzed condition, giving small absorbance variations with respect to the photodegradation test; the effects of adsorption and photolysis were so considered negligible (Figure S2).

3.4. Characterization of Dyes in Single-Dye, Binary, and Ternary Mixtures

As some shift in dye absorbance was noticed when mixing the three dyes, some preliminary evaluations were carried out on the non-degraded solutions to possibly point out the interactions between dyes or influence of variations in solution pH or ionic strength, again possibly induced by the co-presence of multiple dyes.

The stock solutions were used in order to obtain seven equimolar (3×10^{-3} M) solutions, respectively three single-dye solutions, having a concentration of 3×10^{-3} M, three binary mixtures, by mixing the stock solutions (50/50 vol.%, in which each dye has a concentration of 1.5×10^{-3} M), and the ternary mixture, containing all the dyes with a concentration of 10^{-3} M (33 vol.% for each dye).

A preliminary Raman characterization on these solutions did not provide high-quality spectra due to fluorescence or to high signal-to-noise ratio. Therefore, a drop of each solution was deposited on microscope slides and a vacuum pump was used to evaporate the solvent. The so obtained powders were used for Fourier transform Raman (FT-Raman) and Fourier transform infrared (FTIR) analyses.

FT-Raman spectra were acquired using a Nicolet NXR 9650 FT-Raman spectrometer (4 cm^{-1} resolution, Thermo Fisher Scientific, Les Ulis, France) with a 1064 nm laser excitation and power on a powdered sample of about 1 mW. FTIR spectra were collected in transmission mode by depositing powders on a diamond anvil cell and by using a Nicolet Nexus 670 FTIR spectrometer (1 cm^{-1} resolution, Thermo Fisher Scientific, Les Ulis, France).

The effect of acid and alkaline solution pH on the dyes' absorbance spectra was evaluated by adding HCl and NaOH until reaching pH 3 and pH 11.5, respectively, while NaCl (2 M) and Na_2SO_4 (1 M) were chosen to analyze the effect of ionic strength. All chemicals were supplied by Sigma-Aldrich, and absorbance spectra were acquired in the visible range with a spectrophotometer SPECTRONIC 200E (Thermo Fisher Scientific, Les Ulis, France).

4. Results

4.1. Oxide Characterization

Figure 2a shows the top view image of the oxide after anodization. Apparently, a nanoporous morphology rather than a nanotubular one was formed, with the average diameter of the pores equal to 95 nm. However, previous works of our research group [29] reported that single and well-separated TiO_2 nanotubes actually formed below this upper layer with continuous morphology.

Figure 2b shows XRD analyses performed on an anodized titanium sample before and after the annealing treatment at 500°C . The oxide obtained after anodization process is amorphous, while the peaks of anatase and rutile appear only after the calcination process.

According to Spurr [35], the weight fraction of anatase in an anatase–rutile mixed structure can be evaluated as:

$$x_a = \frac{1}{1 + 1.26 \frac{I_R}{I_A}} \quad (12)$$

where I_R and I_A are the strongest XRD reflections for the anatase and rutile phases, located at 2θ of approximately 25.3° (plane (101) of anatase) and 27.4° (plane (110) of rutile).

The results show a predominance of anatase, whereas only small traces of rutile are present (approximately 3%).

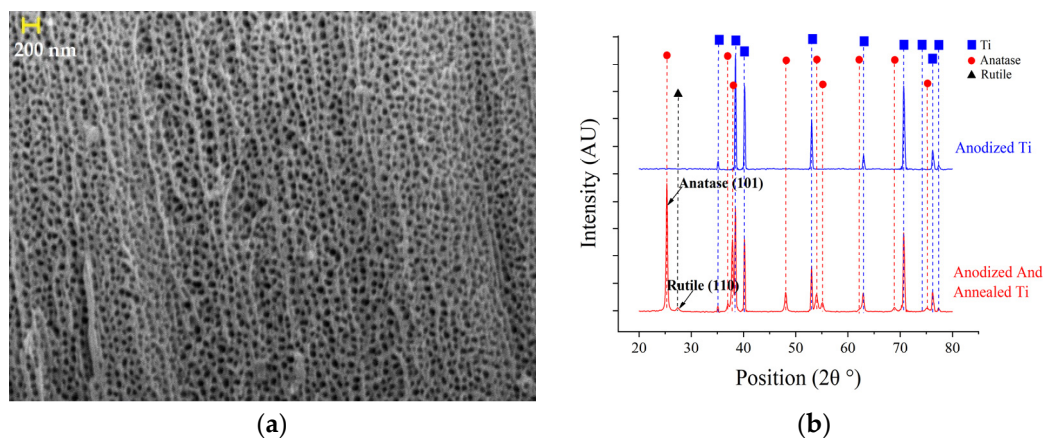


Figure 2. (a) Top-view SEM analyses of the TiO_2 oxide after anodization. (b) XRD analyses of anodized Ti before (top) and after (bottom) annealing treatment.

4.2. Calibration Curves

For all single-dye solutions, the linearity between absorbance and concentration given by the Beer–Lambert law was experimentally confirmed by drawing up the calibration curves (Figure S3). Direct Red 80 ($y = 0.0894x + 0.011$) and Rhodamine B ($y = 0.1031x - 0.003$) show very similar absorptivity, which instead is lower for MB ($y = 0.0628x + 0.0084$). The regression analysis performed produced R^2 values always higher than 0.998, confirming high linearity (Table S4). All intercept values of single-dye calibration curves were negligible.

A Limit Of Detection (LOD) analysis was also performed to identify the smallest concentration measure that can be accepted with confidence and not considered as an erroneous high value of the blank measure [36]:

$$\text{LOD} = 3 \cdot \text{RSE} / m \quad (13)$$

where RSE is the standard error of the estimate of the calibration regression equation and m is its slope. Very low LOD values were found for single dyes, allowing the use of this method down to concentrations of 10^{-7} M (see Table S4).

For the simultaneous analysis of binary solutions, the zero-crossing first-order derivative was used to build up calibration curves and solve spectral interference issues (Figure 3). Firstly, the derivative spectra of single-dye and binary mixtures (Figure 3b,d,f) provided the suitable zero-crossing points; after that, the derivative spectra of solutions listed in Table S2 were used to draw each calibration curve (for details, see Figures S4–S10 in Supplementary Information). Regression analyses were carried out, whose results are summarized in Table S4.

For MB + RhB solutions, a good linear fit was obtained with R^2 values higher than 0.99 and a negligible y-intercept; i.e., $dA/d\lambda$ is indeed linearly proportional to dye concentration according to theory. Even in this case, LOD values were sufficiently low for allowing the use of these curves even for very low dye concentrations. As for DR80 + RhB, R^2 values were sufficiently high (0.9757 and 0.9494). In this case, a lower linearity was expected due to a strong overlap among absorbance spectra; nevertheless, their y-intercept values were again negligible, so that the proportionality among $dA/d\lambda$ and dye concentration was respected. However, LOD values were higher than in the previous case, limiting the range of application of this analytical method down to a concentration of 10^{-6} M. Finally, in MB + DR80, the derivative approach turned out to be unsatisfactory for the evaluation of MB, with poor results in terms of linearity ($R^2 = 0.8095$) and a high intercept value and LOD (Table S4). This was related to the strong shift of the MB maximum peak from 666 nm (single-dye solution) to 690 nm (binary mixture) observed in Figure 3e. Therefore, MB was analyzed at its new maximum peak in

690 nm, where indeed, DR80 absorption was null. In this case, a good calibration was obtained, once again valid only down to 10^{-6} M as indicated by the LOD value (Table S4). Nonetheless, the derivative approach was used for DR80 in the same binary mixture with MB, providing a good linear fit and limit of analytical range of 10^{-6} M. This behavior of MB in the presence of DR80 was unexpected; hence, the above-described Raman analyses were planned and executed to draw some insight into the reasons for this shift (see Section 4.4).

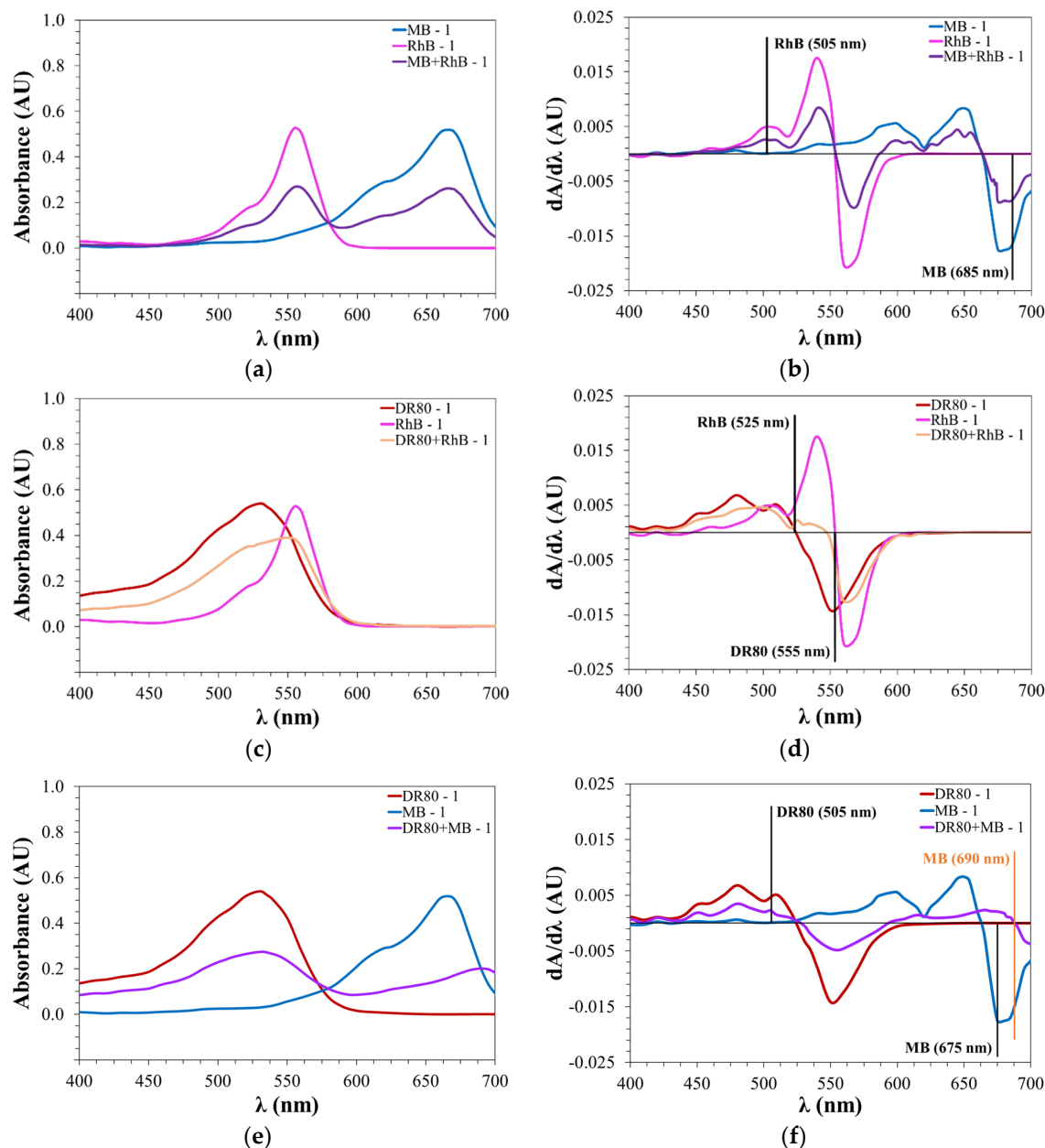


Figure 3. (a) Zero-order spectra of Methylene Blue (MB), Rhodamine B (RhB), and MB + RhB. (b) First-order derivative spectra of MB, RhB, and MB + RhB and their calibration curves. (c) Zero-order spectra of Direct Red 80 (DR80), RhB, and DR80 + RhB. (d) First-order derivative spectra of DR80, RhB, and DR80 + RhB and their calibration curves. (e) Zero-order spectra of DR80, MB, and DR80 + MB. (f) First-order derivative spectra of DR80, MB, and DR80 + MB and their calibration curves. Dye concentrations of the solutions presented in this figure are reported in Tables S1 and S2.

A double divisor ratio spectra derivative approach was used to build up the calibration curves of the ternary solution, and the first-order derivative spectra are presented in Figure 4 and in Figures S11–S13.

Firstly, the comparison among ratio spectra derivative of single dyes (Table S1) and a three-dye system (Table S3) was conducted to obtain the coincident points, i.e., the working wavelengths for the calibration of the dyes. After that, the derivative ratio spectra of the ternary solutions (Table S3) were used for drawing up the calibration curves.

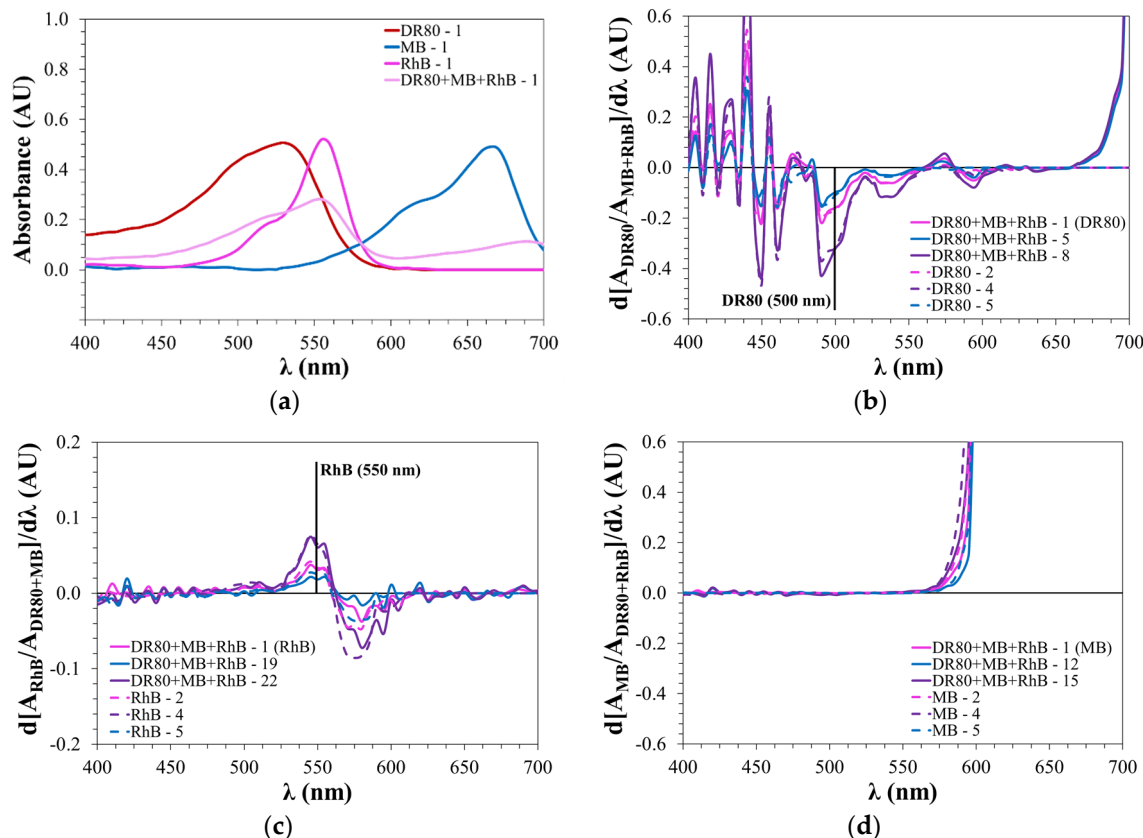


Figure 4. (a) Zero-order spectra of DR80, MB, RhB, and DR80 + MB + RhB solution. (b–d) First derivative of the ratio spectra of dye in single-dye solutions (---) and in ternary solutions having the same molarity of single-dye ones (—). The dye concentrations of the solutions presented in this figure are reported in Tables S1 and S3.

The coincident point of DR80 was identified at 500 nm, where good correspondence was found between derivative spectra in single and ternary solutions (Figure 4b); with similar considerations, the coincident point of RhB was set at 550 nm (Figure 4c).

No coincident point was found for MB. This is not surprising, since the double divisor used in this case had negligible absorbance in the range of 600–700 nm, where MB reaches its maximum; the main consequence is that the ratio spectra, and so even the derivative signals, diverge.

In this case, higher-order ratio spectra derivative signals are not useful, since derivative at higher order provides signals similar to the ones shown in Figure 4d. Due to this reason, MB was directly measured at its maximum peak (690 nm) by simply applying the Beer–Lambert law, as already done for binary mixtures; this is not an issue, since both RhB and DR80 have almost null absorbance at that wavelength.

All calibration curves showed a high linearity, particularly the ones related to DR80 and RhB, with high R^2 values and low y-intercepts. Regarding LOD analysis, DR80 and RhB calibration curves proved to be exploitable up to very low concentrations (10^{-7} M), whereas the curve for MB did not allow clearly distinguishing dye concentration below 10^{-6} M. The regression analysis results are summarized in Table S4.

The accuracy of the three methods was tested by calculating recoveries (%) and errors (%) (Tables S5–S11). The mean recovery values were all close to 100% down to the selected minimum concentrations, with the sole exception of MB + DR80 solutions with low DR80 concentration, where chemical interactions between the two dyes in the presence of a high DR80 concentration are weakened, leading to a gradual shift of MB absorbance peak back to its original value of 666 nm. In general, recovery decreased and error increased with decreasing dye concentration; therefore, kinetics was evaluated before reaching total dye discoloration to guarantee higher data reliability.

4.3. Dyes Degradation

In general, after 3 h irradiation, most dyes are degraded by almost 70%, reaching in some situations (especially when MB is co-present in the solution) an efficiency close to 100% (Figure S14). Although longer exposure times provide increasing photodegradation extents [14], an exposure of three hours was sufficiently high to ensure a minimum of 80% photodegradation, sometimes even reaching 100%, with the only exception of DR80 (60–80%).

As previously mentioned, adsorption tests in dark storage provided negligible results; this was not surprising, considering that the point of zero charge of titanium dioxide lies in a range of 4.5–7 [37] and these tests were carried out at pH 6, thus excluding the presence of strong dye–surface electrostatic interactions. Even more, photolysis tests provided negligible values with respect to the overall process, confirming that dye discoloration was produced by photocatalytic degradation.

Figure 5 reports the first-order kinetics of the studied conditions. These curves show a determination coefficient generally higher than 0.97, reaching maximum values for the starting single-dye solutions (higher than 0.99), confirming that the pseudo-first-order Langmuir–Hinshelwood kinetic model, applied by using Beer–Lambert law, zero-crossing first-order derivative approach, and double divisor ratio spectra derivative method create a good approximation, and that the performed tests had a high repeatability. Kinetic constants calculated through a regression analysis of these photodegradation curves are summarized in Figure 6.

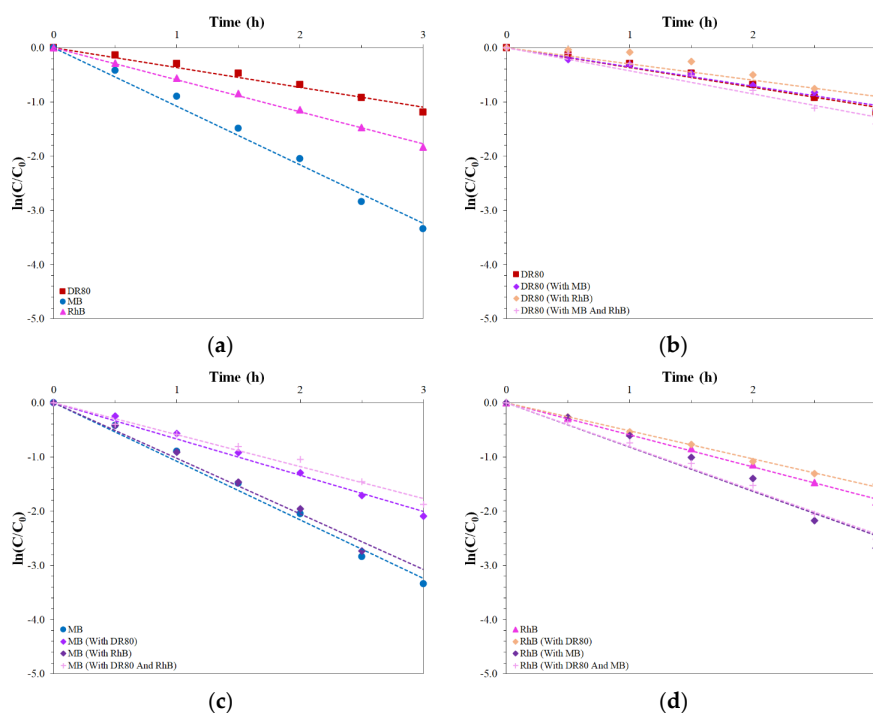


Figure 5. (a) First-order kinetics of single-dye solutions. (b) First-order kinetics of DR80 in the evaluated solutions. (c) First-order kinetics of MB in the evaluated solutions. (d) First-order kinetics of RhB in the evaluated solutions.

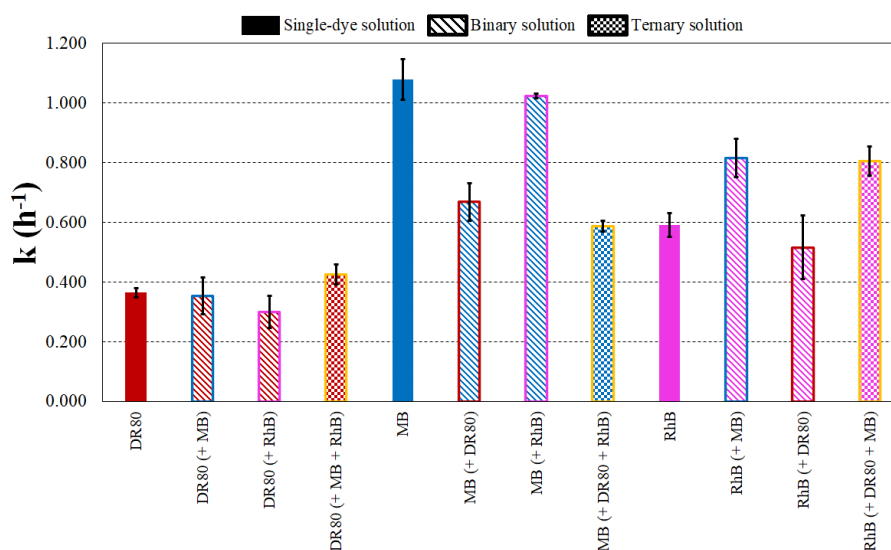


Figure 6. Photocatalysis kinetic constants of the evaluated conditions.

Different dyes in single-dye solutions showed different kinetics; particularly, DR80 discoloration was slower (Figures 5a and 6), whereas MB had the fastest kinetics (Figures 5a and 6). This behavior can be related to the dye structure and molar mass, as reported in the discussion paragraph.

Moreover, interaction among dyes affected photodegradation kinetics. Particularly, DR80 negatively affected the photocatalytic degradation of MB when co-present in the mixture (Figure 5c), with a drastic decrease in MB degradation rate: MB alone degraded by almost 100% in 3 h, but the degradation efficiency decreased by 38% and 45% in the presence of DR80 in the binary and ternary mixture, respectively. On the other hand, DR80 did not show any alteration in the presence of other contaminants (Figure 5b). RhB degradation was enhanced by the addition of MB both in binary and in ternary mixtures (Figure 5d), with a 37% increase of degradation kinetics in both cases. Overall, MB was the most reactive dye in the evaluated solutions, apart from solutions in which DR80 was co-present. Based on the so-obtained results, further analyses were conducted to evidence the cause for these changes in photodegradation efficiency in the binary and ternary mixtures.

4.4. Dyes Characterization

FT-Raman spectra were evaluated by analyzing the main peaks found in the literature for DR80 [38], MB [39–41], and RhB [42,43] (Table S12) and by pointing out the occurrence of specific interactions between molecules, eventually resulting in Raman shifts in the binary and ternary mixtures.

Spectral analysis was conducted on solid-state samples obtained after water evaporation from a drop of the solution deposited on a microscope slide. Due to the low dye concentrations in solution and the concurrent high fluorescence, Raman spectra carried out directly on the solution do not allow the detection of the Raman features of dyes. For this reason, results from solid samples should be taken as indirect evidence of the existence of intermolecular interactions between some of the dye molecules in solution.

MB (Figure 7, Figures S15 and S16) shows a strong fluorescence, particularly in the range 200–800 cm⁻¹ which affects not only the spectra of the single-dye, but also the spectra of mixtures in which MB is co-present, thus increasing the signal-to-noise ratio and reducing the sensitivity for Raman shift analysis.

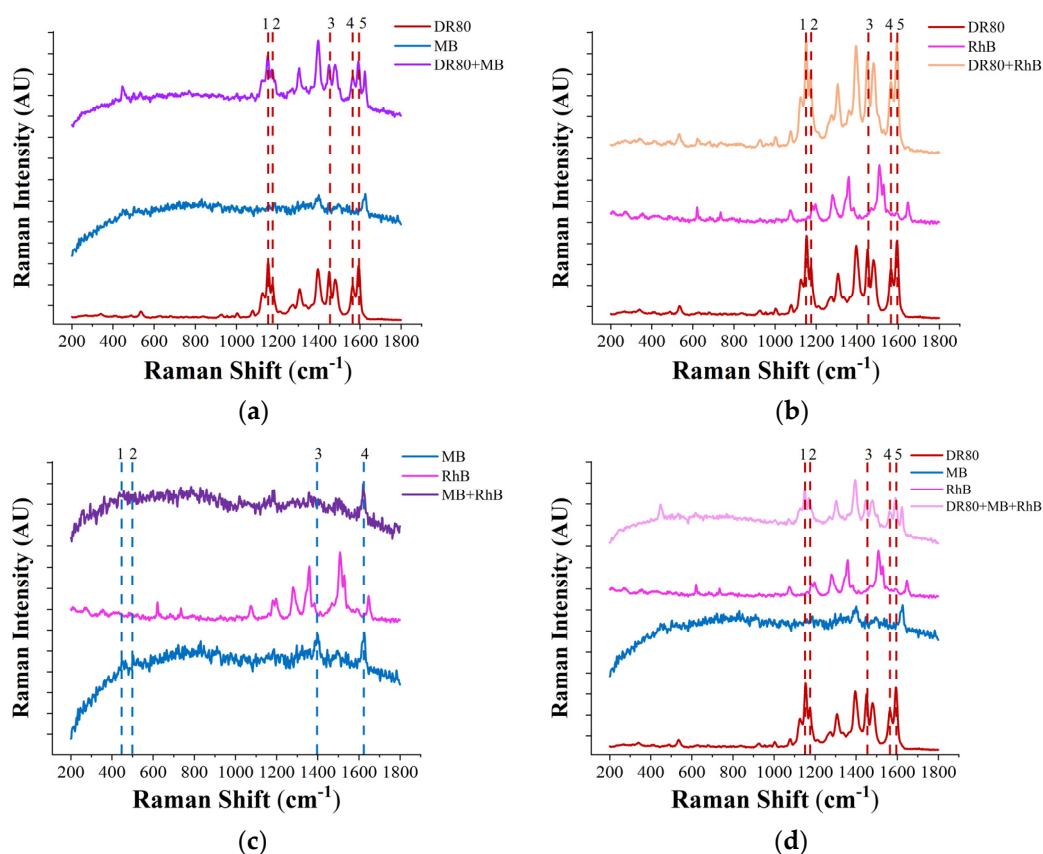


Figure 7. (a) Raman spectra of DR80, MB, and DR80 + MB (peaks of DR80). (b) Raman spectra of DR80, RhB, and DR80 + RhB (peaks of DR80). (c) Raman spectra of MB, RhB, and MB + RhB (peaks of MB). (d) Raman spectra of DR80, MB, RhB, and DR80 + MB + RhB (peaks of DR80).

A negative shift of 3 cm⁻¹ was found for the peaks 1 and 2 of DR80 in all the mixtures in which the dye is co-present (Figure 7a,b,d), suggesting that the stretching vibrational mode of the sulfonate group is affected when another dye is present. Furthermore, a negative shift of 5 cm⁻¹ was found for the peak 4 of MB, whose associated vibrational mode is C–C ring stretching, in MB + RhB binary mixture (Figure 7c), suggesting the presence of an interaction between the two dyes (see Figure S16 to better distinguish MB and DR80 Raman shifts).

Similarly, FTIR spectra were evaluated by measuring the band shift in the binary and ternary mixtures in the main peaks found in the literature for DR80 [38], MB [44,45] and RhB [46–51] (Table S13). The results are reported in Figure 8 and Figures S17–S19. Regarding DR80 + RhB spectra (Figure S18), no evidence of IR shifts were found; thus, the IR spectrum of the binary mixture corresponds to the spectral sum of DR80 and RhB FTIR spectra. Looking at the FTIR spectrum of the ternary solution (Figure S19), the strong overlapping between the peaks does not allow distinguishing clearly the contribution of each dye.

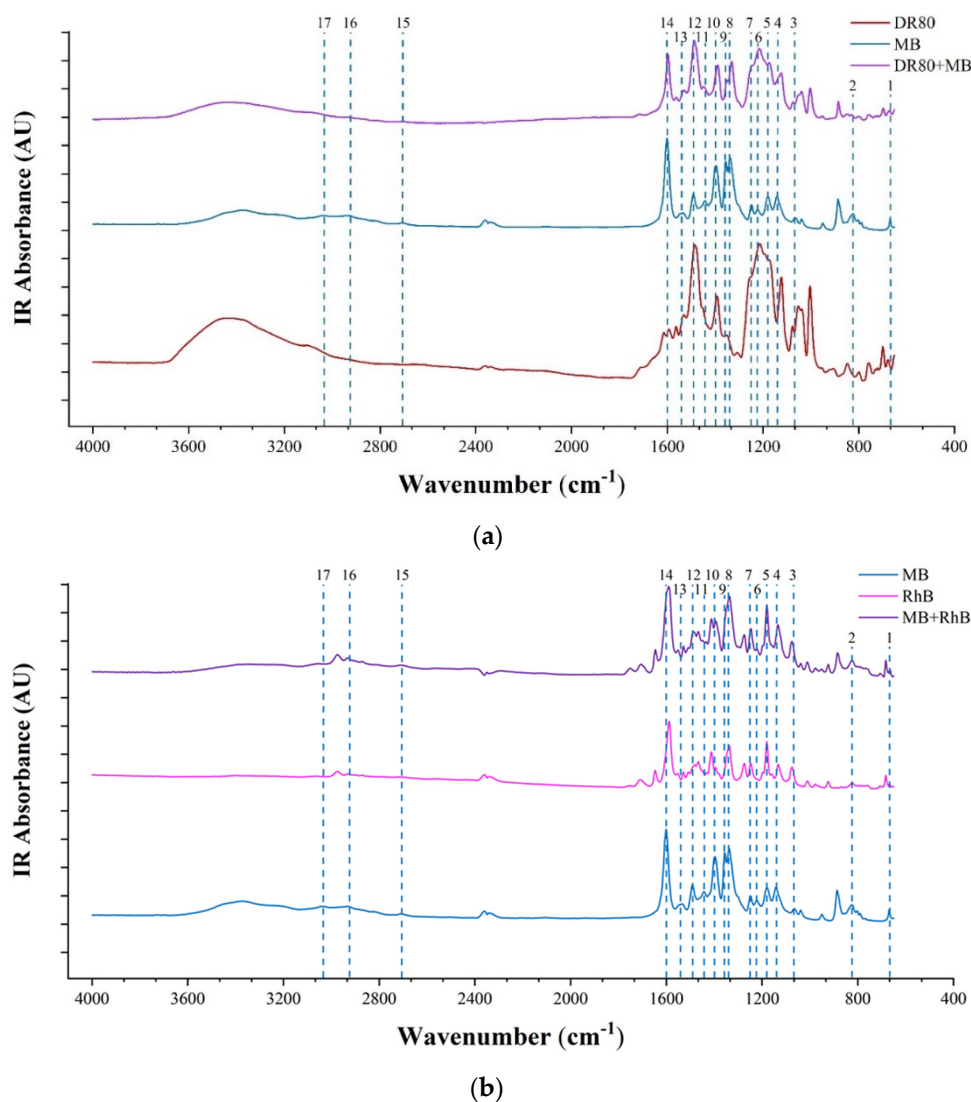


Figure 8. (a) FTIR spectra of DR80, MB, and DR80 + MB (peaks of MB). (b) FTIR spectra of MB, RhB, and MB + RhB (peaks of MB).

On the contrary, weak FTIR shifts were found for specific IR bands of MB both in DR80 + MB and in MB + RhB mixtures. Regarding the first one (Figure 8a), a negative shift was noticed for peaks 8 (8 cm⁻¹), 9 (5 cm⁻¹), 10 (7 cm⁻¹), and 11 (3 cm⁻¹) of MB, which were assigned to C–N stretching, C=S stretching, and C–H in-plane bending (both for peaks 10 and 11), respectively. By comparing the FTIR spectrum of DR80 + MB and the spectral sum obtained by the FTIR spectra of pure DR80 and MB, it was verified that these shifts are not related to trivial effects on the band's shape, due to the superposition of absorption features of the two different species in the same spectral region. Indeed, the observed shifts prove the presence of weak interactions between these two dyes.

Regarding MB in MB + RhB mixture (Figure 8b), negative shifts were found in peak 1 (5 cm⁻¹), peak 10 (4 cm⁻¹), and peak 12 (7 cm⁻¹), corresponding to C–S–C and C–N stretching, C–H in-plane bending, and C=S stretching.

Even if the evidence of interactions among these dyes is quite weak, the spectral comparison between MB + RhB FTIR spectrum and the spectral sum of the two dyes assures that these shifts are not determined by the spectral sum, but they rather reflect some interactions between the two dyes.

These observations could motivate the changes in degradation rate observed for MB in the presence of DR80 and for RhB in the presence of MB, which can then be ascribed to dye interactions, either suppressing (MB + DR80) or enhancing (MB + RhB) degradation. On the other hand, the

analysis of the absorption spectra in the visible range of binary and ternary mixtures showed a clear modification of the electronic structure of MB when involved in binary solution with DR80 (Figure 3e) or in ternary solutions (Figure 4a), as indicated by the non-negligible shift (about 20 nm) of its main absorption band that is not related to trivial effects due to spectra superposition.

To investigate whether the observed shifts of the dyes' absorption features in binary and ternary solutions are related to specific intermolecular interactions between the dye molecules, the possible solvatochromism of these dyes was investigated. In particular, the effects of acidic and basic pH, together with the addition of salts (NaCl and Na₂SO₄) was also analyzed for each solution. The absorbance spectra acquired in the visible range for single-dye and binary mixtures are reported in Figure 9, whereas the ternary mixture ones are shown in Figure S20.

Both pH and salts addition have no effect on DR80 (Figure 9a); RhB is affected only by acidic conditions (Figure 9c), with a shift of the maximum absorbance peak from 555 to 560 nm and an enhancement of its absorbance. MB absorbance spectrum (Figure 9b) is not affected by acidic and basic pH, as this dye is stable in aqueous solutions between pH 2 and 12 [52]. On the other hand, for MB both in single-dye solution and with RhB, the addition of both NaCl and Na₂SO₄ results in an absorbance decrease at the maximum peak at 666 nm, together with an increase of the shoulder at 610 nm and a slight redshift of RhB absorbance peak in the binary mixture (Figure 9f).

In the DR80 + MB mixture (Figure 9d), the shift of MB peak from 666 to 690 nm is further modified in the presence of salts, leading to a redshift of MB peak up to the range 695–700 nm and a considerable variation of DR80 contribution to the absorbance spectrum.

As for the DR80 + RhB mixture (Figure 9e), the addition of salts causes a redshift of the whole absorbance spectra of about 10 nm in the range 450–540 nm and a lighter shift (5 nm) in the range 555–610 nm, including the RhB peak.

Ternary solutions (Figure S20), being constituted by the three different dyes, are affected by both salts addition and acidic condition; the only solution that behaves similarly to the neutral condition is the basic pH solution, since neither single-dye nor binary mixtures seem to be affected by basicity.

In conclusion, some changes of the dyes' spectral pattern observed while adding salts or changing the pH of the solution are often clearly detectable. However, the observed shifts of the main absorption peak of MB are very small in comparison with the redshift of the band observed in the presence of DR80, thus suggesting that different dyes can specifically interact in solution.

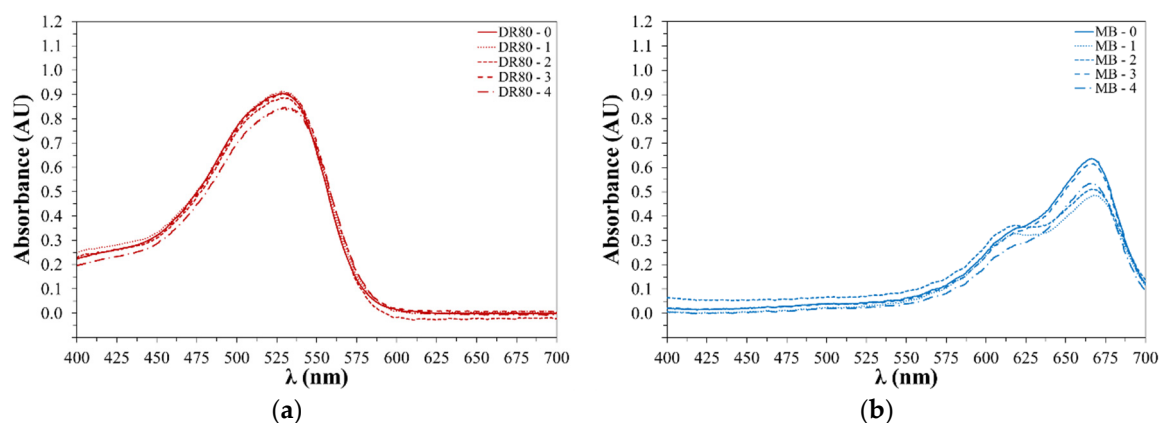


Figure 9. Cont.

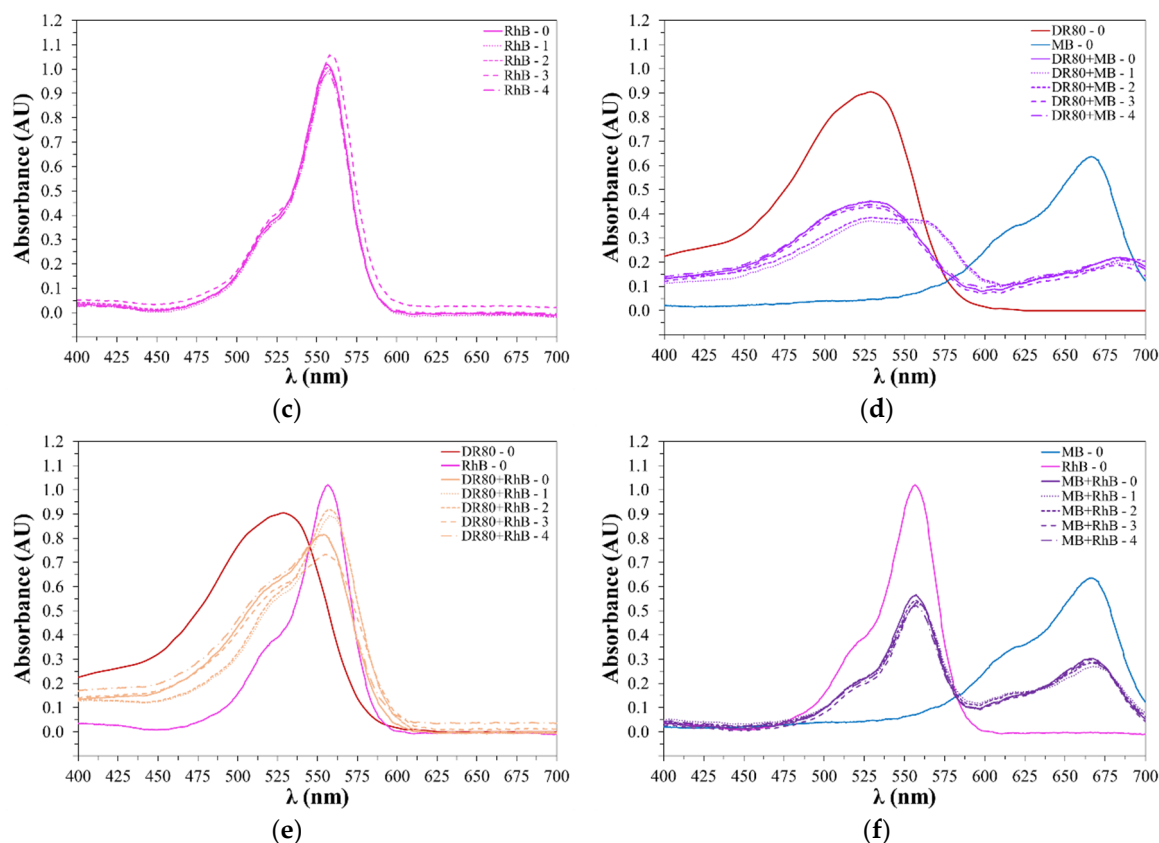


Figure 9. Absorbance spectra of DR80 (a), MB (b), RhB (c), DR80 + MB together with DR80 and MB single-dye solutions (d), DR80 + RhB together with DR80 and RhB single-dye solutions (e), and MB + RhB together with MB and RhB single-dye solutions (f). 0 refers to pH 6 solution, without the addition of salts; 1 refers to pH 6 solution with the addition of 2 M of NaCl; 2 refers to pH 6 solution with the addition of 1 M of Na_2SO_4 ; 3 refers to acidic solution (pH 2.5–3); 4 refers to basic solution (pH 11.5–12).

5. Discussion

On a general basis, in all evaluated cases, high photodegradation efficiencies were obtained, thus supporting the use of nanotubular TiO_2 as a photocatalyst for dye degradation, also in complex mixed effluents. All the solutions in which DR80 is not present show higher efficiency, thus indicating that the presence of DR80 decreases the efficacy of the proposed photocatalyst. This effect is more evident by looking at the amount of degraded mass (Figure 10).

In MB and RhB single-dye solution, together with their binary mixtures, the degraded mass with respect to the initial one is always higher than 83%, whereas as the amount of DR80 increases, the efficiency decreases, passing from 80% of degraded dye in the ternary mixture (passing from 0.30 mg of initial dye to 0.06 mg of non-degraded dye) to 71.9% of degraded dye in DR80 + MB (from 0.32 to 0.09 mg). Indeed, as solutions are equimolar, but DR80 molecular weight is more than double the RhB one, and almost 4 times that of MB, the weight of dye to be degraded varies from one solution to another, and an increase in the quantity of mass to be degraded leads to a rise of discoloration time. Looking at this same concept from a dye structure viewpoint, the total amount of photogenerated radicals needed for the mineralization of dyes may change from dye to dye due to their different molecular weight. Even the presence of interactions among dyes may affect photodegradation kinetics; in fact, although DR80 + RhB is made up of a greater initial mass, the percentage of degraded mass is still higher than DR80 + MB due to the drastic decrease of MB photocatalytic degradation kinetics when DR80 is co-present in the solution.

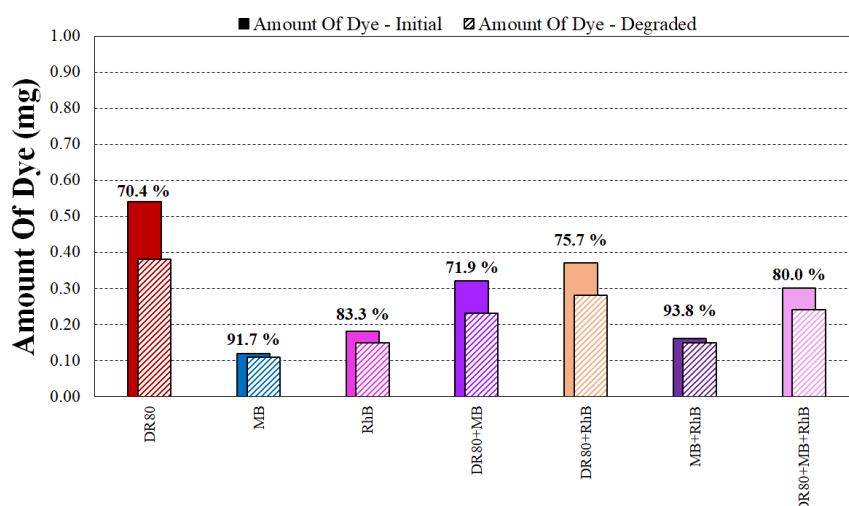


Figure 10. Amount of initial dye and degraded dye for each studied condition (the bold values refer to the percentage of degraded mass).

As previously mentioned, the different kinetics observed relate to dye structure. The chemical structure of a dye (as more specifically addressed in the following) can make it more or less recalcitrant to oxidation; moreover, steric effects should be taken into account, affecting dye adsorption on TiO_2 surface, which is known to strongly influence photodegradation as well, as it is one of the required steps for dye degradation. We here propose a description of each dye and then summarized by outlining some considerations:

- Direct Red 80 is a tetra-azo dye with a strong absorbance in the UV-Visible region that is characterized by four azo bonds ($-\text{N}=\text{N}-$); these constitute not only its chromophores, but also its weak points, where the molecule is more easily broken by photogenerated radicals. This dye is also characterized by the presence of six sulfonic groups ($-\text{SO}_3^-$) that enhance its solubility [53]. The high molecular weight ($1373.07 \text{ g}\cdot\text{mol}^{-1}$) and the large amount of benzene and naphthalene rings suggest a difficult mineralization, as indeed observed, especially if compared with MB and RhB.
- Methylene Blue is a heterocycle dye characterized by a chromophore thiazine group ($-\text{C}=\text{N}-$ and $-\text{C}=\text{S}-$ bonds) [54], which represents the most active site for radical oxidation. Its molecular mass is the lowest among the evaluated dyes ($319.85 \text{ g}\cdot\text{mol}^{-1}$), which explains its faster photodegradation.
- Rhodamine B ($479.01 \text{ g}\cdot\text{mol}^{-1}$) is a triphenylmethane dye characterized by the presence of a conjugated xanthene group (which is in turn bonded to four N-ethyl groups) [55]. This chromophore results in one of the most photoactive sites during photodegradation by radical species.

It has been reported [56,57] that an increased number of azo bonds involves longer discoloration time, significantly affecting the photodegradation rate. This is evident for DR80, which turns out to be the most recalcitrant dye due to the four $-\text{N}=\text{N}-$ bonds [57,58]; still, the presence of sulfonic groups enhances its solubility, promoting chemical interactions with photogenerated hydroxyl radicals and mitigating the effect of azo bonds.

On the other hand, RhB and MB structures do not contain any azo groups, which explains their faster degradation. Moreover, the fastest kinetics was shown by MB: this can be related to the presence of thiazine groups ($-\text{C}=\text{S}-$ and $-\text{C}=\text{N}-$ bonds), which favor bond cleavage, while the carboxylate anion in RhB enhances steric repulsion and partially impairs its adsorption on the photocatalyst surface [59].

In the following, the possible degradation pathways for each of the evaluated dye are reported:

- Direct Red 80 is supposed to degrade starting from the azo bond cleavage, followed by desulfonation and dihydroxylation, thus forming aromatic compounds that may mineralize in CO_2 , H_2O , SO_4^{2-} , and NH_3 [60].
- Methylene Blue is supposed to degrade through different reaction pathways, starting from the thiazine group opening with $-\text{C}=\text{S}-$ and $-\text{C}=\text{N}-$ bond cleavage, passing through desulfonation and deamination, eventually mineralizing in CO_2 , H_2O , SO_4^{2-} and amine by-products [54].
- Regarding RhB, no proof of N-de-ethylation was found, since discoloration took place without the evidence of an absorbance peak shift from 555 to 500–520 nm, which is typical of this phenomenon [11]. Hence, it is assumed that degradation is linked to cleavage of the conjugated xanthene group, followed by deamination and dihydroxylation, which may lead to the formation of CO_2 , H_2O , and amine by-products [55,61].

While these behaviors are consolidated when only one of the specified dyes is present, interactions may take place in mixed solutions. To evaluate this, calibration curves were first analyzed. No alteration in slope was observed in RhB + DR80 mixtures; moreover, degradation kinetics did not show any variation from single-dye solutions, indeed confirming the absence of interactions between these dyes. On the other hand, there was a 12% decrease in the slope of the RhB calibration curve when mixed with MB. A corresponding change in the degradation kinetics of RhB in the presence of MB confirms possible chemical interactions among these two dyes; conversely, MB seemed not to be affected.

The most evident interaction is related to MB in the DR80 + MB mixture, with a shift of MB absorbance peak in the presence of DR80 from 666 to 690 nm and a 26% decrease of the MB calibration curve slope, indicating an equivalent reduction in absorptivity coefficient. These findings were accompanied by a decrease in the degradation kinetics of MB in the presence of DR80 (Figure 6).

The mentioned modifications in dye behavior were related to possible interactions between dyes, since other effects such as concentration variations or quantum yield variations were excluded.

In fact, each dye in binary and ternary mixtures is contained in decreased concentration compared to the single solutions (respectively 5×10^{-6} M and 3.3×10^{-6} M), which should enhance degradation (see Figure S21); however, for MB, a worsening was observed, thus excluding an effect of dye concentration on photodegradation kinetics.

On the other hand, quantum yield could vary on account of the different overall light absorbance of each dye, hence leaving a smaller amount of light available at the catalyst surface for photoactivation. To evaluate this aspect, an analysis of light absorbance from the different dyes was also performed. Considering that the UV LED has its maximum emission peak in the range of 350–390 nm and each dye absorbs UV light differently (Figure S22), for this analysis, a new parameter has been introduced, the Absorbance Relative Index (ARI), whose value (arbitrary units) was evaluated through the following equation:

$$\text{ARI (AU)} = \sum_{340}^{700} A_{n,i} \cdot E_{r,i} \quad (14)$$

where $A_{n,i}$ is the normalized absorbance with respect to the maximum measured absorbance (1.030 AU for Rhodamine B at 555 nm in its single-dye solution) at wavelength i , and $E_{r,i}$ is the relative emission power of the UV lamp (maximum value equal to 1 at 365 nm) at wavelength i . Even though this parameter does not have a physical meaning, it allows comparing light absorption by the different solutions in our specific system.

Direct Red 80 is the dye that most absorbs UV, and its absorption decreases as the dye concentration decreases (Figure S23). Instead, MB had negligible ARI, and RhB had an intermediate behavior, closer to MB. While solutions containing DR80 actually reduce the amount of light available for photocatalyst activation, and hence the quantum yield of the overall system, the ARI does not correlate with the photocatalytic reaction rate in dye mixtures, as DR80 slows down MB degradation but not the RhB one.

In order to verify the occurrence of dye interactions, FTIR, FT-Raman, and visible spectrophotometry analyses were conducted.

FT-Raman and FTIR analyses proved that there are some interactions among dyes; in particular, FT-Raman proved that the stretching vibrational mode of the DR80 sulfonate group is shifted when other dyes are co-present, whereas the C–C stretching of MB seems to be affected by the presence of RhB. On the other side, FTIR proved that C–N stretching, C=S stretching and C–H in-plane bending vibrational modes of MB in DR80 + MB mixture are negatively shifted. These findings can be justified by interactions between the DR80 sulfonate group and MB C–N bond of the dimethylamino group and C=S bond of the thiazine group; the latter in particular is the most active site of MB for radical oxidation, which suggests that this may affect the photocatalytic degradation, as indeed proved by our results.

On the other hand, also the absorption spectra of the mixtures indicate that MB is affected by the presence of other dyes, showing a shift of the MB absorption maximum from 666 to 690 nm (DR80 + MB). While some changes in absorbance spectra related to pH changes or the addition of ionic species into the solution were observed (Figure 9), thus demonstrating that these dyes are quite sensitive to the environment, the observed peaks shifts are always very small if compared to those occurring in binary and ternary solutions.

These observations suggest that dyes specifically interact among them in solution, so that dyes are arranged according to a preferential geometry due to the electrostatic forces among them; as a consequence, these specific interactions can modify the photodegradation kinetics of binary and ternary mixtures.

6. Conclusions

We presented the application of nanotubular TiO₂ films for the photocatalytic degradation of multi-dye aqueous solutions. Generally, the results show that most dyes and dye mixtures degrade by more than 80%, confirming that titanium dioxide nanotubes are an efficient photocatalyst not only against simple dyes, but also in the treatment of complex effluents. Moreover, the three different spectrophotometric approaches were suitable for the analysis of multi-dye systems.

DR80 demonstrated to degrade with similar kinetics independent of the co-presence of other chemical compounds, both in binary and in ternary mixtures. Conversely, the presence of multiple dyes affected the MB and RhB degradation rates, leading to an enhancement or a worsening of the reaction rate. An in-depth analysis allowed relating this behavior to specific interactions among dyes. Hence, when designing and evaluating a catalyst for real wastewaters where multiple contaminants are present, interactions among dyes and with other salts present in the effluent should be considered, as they may affect the kinetics of the photocatalytic process.

Supplementary Materials: The following are available online at <http://www.mdpi.com/2079-6412/10/10/919/s1>, Figure S1: (a) Schematic representation of the batch reactor used in this study (the TiO₂ nanotubular array is photoactivated by the LED positioned on top, at 3 cm from it). (b) Photograph of the batch reactor used in this study (it is possible to distinguish the beaker containing the solutions, the sample, the sample holder on which the sample is positioned, the magnetic stirrer, and the 3D printed component that covers the beaker and supports the UV LED). Figure S2: Kinetics of photocatalysis, photolysis and adsorption in the evaluated conditions ("PC" stands for photocatalysis). Figure S3: Calibration curves for dyes in single-dye solutions. Figure S4: First-order derivative spectra of DR80, MB and DR80 + MB, at different DR80 concentrations, together with DR80 calibration curve. Dye concentrations of the solutions presented in this figure are reported in Tables S1 and S2. Figure S5: First-order derivative spectra of DR80, MB and DR80 + MB, at different MB concentrations, together with MB calibration curve. Dye concentrations of the solutions presented in this Figure are reported in Tables S1 and S2. Figure S6: MB calibration curve in DR80 + MB system, evaluated at MB maximum absorbance peak (690 nm). Figure S7: First-order derivative spectra of DR80, RhB and DR80 + RhB, at different DR80 concentrations, together with DR80 calibration curve. Dye concentrations of the solutions presented in this figure are reported in Tables S1 and S2. Figure S8: First-order derivative spectra of DR80, RhB and DR80 + RhB, at different RhB concentrations, together with RhB calibration curve. Dye concentrations of the solutions presented in this figure are reported in Tables S1 and S2. Figure S9: First-order derivative spectra of MB, RhB, and MB + RhB, at different MB concentrations, together with MB calibration curve. Dye concentrations of the solutions presented in this figure are reported in Tables S1 and S2. Figure S10: First-order derivative spectra of MB, RhB, and MB + RhB, at different RhB concentrations, together with RhB calibration curve. Dye concentrations of the solutions presented in this figure are reported in Tables S1 and S2. Figure S11: First-order derivative spectra of DR80 and DR80 + MB + RhB at different DR80 concentrations, together with DR80 calibration curve. Dye concentrations of the solutions

presented in this figure are reported in Tables S1 and S3. Figure S12: First-order derivative spectra of DR80 and DR80 + MB + RhB, at different RhB concentrations, together with RhB calibration curve. Dye concentrations of the solutions presented in this figure are reported in Tables S1 and S3. Figure S13: MB calibration curve in DR80 + MB + RhB system, evaluated at MB maximum absorbance peak (690 nm). Figure S14: Photocatalytic efficiency for the evaluated conditions. Figure S15: (a) Raman spectra of DR80, MB and DR80 + MB (dashed lines indicate peaks of MB). (b) Raman spectra of DR80, RhB, and DR80 + RhB (dashed lines indicate peaks of RhB). (c) Raman spectra of MB, RhB, and MB + RhB (dashed lines indicate peaks of RhB). (d) Raman spectra of DR80, MB, RhB, and DR80 + MB + RhB (dashed lines indicate peaks of MB). (e) Raman spectra of DR80, MB, RhB, and DR80 + MB + RhB (dashed lines indicate peaks of RhB). Figure S16: (a) Raman spectra of DR80, MB, and DR80 + MB (peaks of DR80, zoom in the range 1100–1700 cm^{-1}). (b) Raman spectra of DR80, RhB, and DR80 + RhB (peaks of DR80, zoom in the range 1100–1700 cm^{-1}). (c) Raman spectra of MB, RhB, and MB + RhB (peaks of MB, zoom in the range 1100–1700 cm^{-1}). (d) Raman spectra of DR80, MB, RhB, and DR80 + MB + RhB (peaks of DR80, zoom in the range 1100–1700 cm^{-1}). Figure S17: (a) FTIR spectra of DR80, MB, and DR80 + MB (dashed lines indicate peaks of DR80). (b) FTIR spectra of MB, RhB, and MB + RhB (dashed lines indicate peaks of RhB). Figure S18: (a) FTIR spectra of DR80, RhB, and DR80 + RhB (dashed lines indicate peaks of DR80). (b) FTIR spectra of DR80, RhB, and DR80 + RhB (dashed lines indicate peaks of RhB). Figure S19: (a) FTIR spectra of DR80, MB, RhB, and DR80 + MB + RhB (dashed lines indicate peaks of DR80). (b) FTIR spectra of DR80, MB, RhB, and DR80 + MB + RhB (dashed lines indicate peaks of MB). (c) FTIR spectra of DR80, MB, RhB, and DR80 + MB + RhB (dashed lines indicate peaks of RhB). Figure S20: Absorbance spectra of DR80 + MB + RhB and single-dye solutions. 0 refers to pH 6 solution, without the addition of salts; 1 refers to pH 6 solution with the addition of 2 M of NaCl; 2 refers to pH 6 solution with the addition of 1 M of Na_2SO_4 ; 3 refers to acidic solution (pH 2.5–3); 4 refers to basic solution (pH 11.5–12). Figure S21: Photocatalytic kinetics of both the studied conditions and single-dye solutions with concentration 3.3×10^{-6} M. Figure S22: Relative emission power of the UV LED (black line); the dotted lines refers to the absorbance of DR80, MB, and RhB in the range 350–1000 nm. Figure S23: Absorbance relative index (ARI) for the evaluated conditions. Table S1: Solutions used for DR80, MB, and RhB calibration in single-dye solution (underlined) and for the analysis of coincident points in ternary solutions (the theoretical concentration C_t is expressed in 10^{-6} M). Table S2: Binary solutions used for DR80, MB, and RhB calibration in binary mixture (the theoretical concentration C_t is expressed in 10^{-6} M). Table S3: Ternary solutions used for DR80, MB, and RhB calibration in DR80 + MB + RhB solution (the theoretical concentration C_t is expressed in 10^{-6} M). Table S4: Regression analysis for the calibration curves in single-dye, binary, and ternary mixtures (S.E. = standard error, RSE = standard error of the estimate). Table S5: Analysis of accuracy for DR80 in single-dye solution (the theoretical concentration C_t and the measured concentration C_m are expressed in 10^{-6} M). Table S6: Analysis of accuracy for MB in single-dye solution (the theoretical concentration C_t and the measured concentration C_m are expressed in 10^{-6} M). Table S7: Analysis of accuracy for RhB in single-dye solution (the theoretical concentration C_t and the measured concentration C_m are expressed in 10^{-6} M). Table S8: Analysis of accuracy for DR80 + MB (the theoretical concentration C_t and the measured concentration C_m are expressed in 10^{-6} M). Table S9: Analysis of accuracy for DR80 + RhB (the theoretical concentration C_t and the measured concentration C_m are expressed in 10^{-6} M). Table S10: Analysis of accuracy for MB + RhB (the theoretical concentration C_t and the measured concentration C_m are expressed in 10^{-6} M). Table S11: Analysis of accuracy for DR80 + MB + RhB (the theoretical concentration C_t and the measured concentration C_m are expressed in 10^{-6} M). Table S12: Raman band assignments of selected marker bands of DR80, MB and RhB (Raman shift is expressed in cm^{-1}). Table S13: The characteristic frequencies of FTIR bands of DR80, MB and RhB (FTIR band is expressed in cm^{-1}).

Author Contributions: Conceptualization, U.B., M.V.D., and M.P.; methodology, U.B., M.V.D., C.C., and A.L.; validation, M.V.D., C.C., and M.O.; formal analysis, U.B. and A.L.; investigation, U.B., F.P., and A.L.; resources, M.P. and M.O.; data curation, U.B.; writing—original draft preparation, U.B.; writing—review and editing, M.V.D., C.C., and A.L.; supervision, M.P. and M.V.D.; project administration: M.V.D. All authors have read and agreed to the published version of the manuscript.

Funding: No specific funding was used in this work.

Conflicts of Interest: The authors declare no conflict of interest.

References

1. Rueda-Marquez, J.J.; Levchuk, I.; Fernández Ibañez, P.; Sillanpää, M. A critical review on application of photocatalysis for toxicity reduction of real wastewaters. *J. Clean. Prod.* **2020**, *258*, 120694. [\[CrossRef\]](#)
2. Al-Mamun, M.R.; Kader, S.; Islam, M.S.; Khan, M.Z.H. Photocatalytic activity improvement and application of UV-TiO₂ photocatalysis in textile wastewater treatment: A review. *J. Environ. Chem. Eng.* **2019**, *7*, 103248. [\[CrossRef\]](#)
3. Byrne, C.; Subramanian, G.; Pillai, S.C. Recent advances in photocatalysis for environmental applications. *J. Environ. Chem. Eng.* **2018**, *6*, 3531–3555. [\[CrossRef\]](#)

4. Humayun, M.; Raziq, F.; Khan, A.; Luo, W. Modification strategies of TiO₂ for potential applications in photocatalysis: A critical review. *Green Chem. Lett. Rev.* **2018**, *11*, 86–102. [\[CrossRef\]](#)
5. Haider, A.J.; Jameel, Z.N.; Al-Hussaini, I.H.M. Review on: Titanium dioxide applications. *Energy Procedia* **2019**, *157*, 17–29. [\[CrossRef\]](#)
6. Diamanti, M.V.; Del Curto, B.; Pedferri, M.P. Anodic oxidation of titanium: From technical aspects to biomedical applications. *J. Appl. Biomater. Biomech.* **2011**, *9*, 55–69. [\[CrossRef\]](#)
7. Boyjoo, Y.; Sun, H.; Liu, J.; Pareek, V.K.; Wang, S. A review on photocatalysis for air treatment: From catalyst development to reactor design. *Chem. Eng. J.* **2017**, *310*, 537–559. [\[CrossRef\]](#)
8. Rao, B.M.; Torabi, A.; Varghese, O.K. Anodically grown functional oxide nanotubes and applications. *MRS Commun.* **2016**, *6*, 375–396. [\[CrossRef\]](#)
9. Paramasivam, I.; Jha, H.; Liu, N.; Schmuki, P. A review of photocatalysis using self-organized TiO₂ nanotubes and other ordered oxide nanostructures. *Small* **2012**, *8*, 3073–3103. [\[CrossRef\]](#)
10. Diamanti, M.V.; Ormellese, M.; Pedferri, M.P. Application-wise nanostructuring of anodic films on titanium: A review. *J. Exp. Nanosci.* **2015**, *10*, 1285–1308. [\[CrossRef\]](#)
11. Diamanti, M.V.; Ormellese, M.; Marin, E.; Lanzutti, A.; Mele, A.; Pedferri, M.P. Anodic titanium oxide as immobilized photocatalyst in UV or visible light devices. *J. Hazard. Mater.* **2011**, *186*, 2103–2109. [\[CrossRef\]](#) [\[PubMed\]](#)
12. Santamaria, M.; Conigliaro, G.; Di Franco, F.; Megna, B.; Di Quarto, F. Electronic properties of thermal oxides on Ti and their influence on impedance and photoelectrochemical behavior of TiO₂ nanotubes. *J. Electrochem. Soc.* **2017**, *164*, C113–C120. [\[CrossRef\]](#)
13. Berger, S.; Albu, S.P.; Schmidt-Stein, F.; Hildebrand, H.; Schmuki, P.; Hammond, J.S.; Paul, D.F.; Reichlmaier, S. The origin for tubular growth of TiO₂ nanotubes: A fluoride rich layer between tube-walls. *Surf. Sci.* **2011**, *605*, L57–L60. [\[CrossRef\]](#)
14. Bellè, U.; De Flaviis, L.; Diamanti, M.V.; Ormellese, M.; Pedferri, M.P. Photocatalytic activity of immobilized nano-TiO₂ in complex wastewaters: Case study of multiple dye composition. In Proceedings of the TechConnect World Innovation Conference & Expo, Boston, MA, USA, 17–19 June 2019; pp. 201–204.
15. Kucharska, M.; Grabka, J. A review of chromatographic methods for determination of synthetic food dyes. *Talanta* **2010**, *80*, 1045–1051. [\[CrossRef\]](#)
16. Arnault, I.; Christidès, J.P.; Mandon, N.; Haffner, T.; Kahane, R.; Auger, J. High-performance ion-pair chromatography method for simultaneous analysis of alliin, deoxyalliin, allicin and dipeptide precursors in garlic products using multiple mass spectrometry and UV detection. *J. Chromatogr. A* **2003**, *991*, 69–75. [\[CrossRef\]](#)
17. Peralta-Zamora, P.; Kunz, A.; Nagata, N.; Poppi, R.J. Spectrophotometric determination of organic dye mixtures by using multivariate calibration. *Talanta* **1998**, *47*, 77–84. [\[CrossRef\]](#)
18. Gao, J.F.; Wang, J.H.; Yang, C.; Wang, S.Y.; Peng, Y.Z. Binary biosorption of ACID RED 14 and Reactive Red 15 onto acid treated okara: Simultaneous spectrophotometric determination of two dyes using partial least squares regression. *Chem. Eng. J.* **2011**, *171*, 967–975. [\[CrossRef\]](#)
19. Al-Degs, Y.S. Determination of three dyes in commercial soft drinks using HLA/GO and liquid chromatography. *Food Chem.* **2009**, *117*, 485–490. [\[CrossRef\]](#)
20. Andronic, L.; Duta, A. Photodegradation processes in two-dyes systems-Simultaneous analysis by first-order spectra derivative method. *Chem. Eng. J.* **2012**, *198–199*, 468–475. [\[CrossRef\]](#)
21. Mem, H.; Ma, M. Novel and facile spectrophotometric techniques for the determination of sofosbuvir and ledipasvir in their tablet dosage form. *J. Anal. Pharm. Res.* **2018**, *7*, 92–99. [\[CrossRef\]](#)
22. Karpińska, J. Derivative spectrophotometry—Recent applications and directions of developments. *Talanta* **2004**, *64*, 801–822. [\[CrossRef\]](#) [\[PubMed\]](#)
23. Bosch Ojeda, C.; Sanchez Rojas, F. Recent developments in derivative ultraviolet/visible absorption spectrophotometry. *Anal. Chim. Acta* **2004**, *518*, 1–24. [\[CrossRef\]](#)
24. Dinç, E. The spectrophotometric multicomponent analysis of a ternary mixture of ascorbic acid, acetylsalicylic acid and paracetamol by the double divisor-ratio spectra derivative and ratio spectra-zero crossing methods. *Talanta* **1999**, *48*, 1145–1157. [\[CrossRef\]](#)
25. Dinç, E.; Baydan, E.; Kanbur, M.; Onur, F. Spectrophotometric multicomponent determination of sunset yellow, tartrazine and allura red in soft drink powder by double divisor-ratio spectra derivative, inverse least-squares and principal component regression methods. *Talanta* **2002**, *58*, 579–594. [\[CrossRef\]](#)

26. Salinas, F.; Nevado, J.J.B.; Mansilla, A.E. A new spectrophotometric method for quantitative multicomponent analysis resolution of mixtures of salicylic and salicyluric acids. *Talanta* **1990**, *37*, 347–351. [\[CrossRef\]](#)
27. Nevado, J.J.B.; Cabanillas, C.G.; Salinas, F. Spectrophotometric resolution of ternary mixtures of salicylaldehyde, 3-hydroxybenzaldehyde and 4-hydroxybenzaldehyde by the derivative ratio spectrum-zero crossing method. *Talanta* **1992**, *39*, 547–553. [\[CrossRef\]](#)
28. Houas, A.; Lachheb, H.; Ksibi, M.; Elaloui, E.; Guillard, C.; Herrmann, J.M. Photocatalytic degradation pathway of methylene blue in water. *Appl. Catal. B Environ.* **2001**, *31*, 145–157. [\[CrossRef\]](#)
29. Arenas, B.E.S.; Strini, A.; Schiavi, L.; Bassi, A.L.; Russo, V.; Del Curto, B.; Diamanti, M.V.; Peddeferri, M.P. Photocatalytic activity of nanotubular TiO₂ films obtained by anodic oxidation: A comparison in gas and liquid phase. *Materials* **2018**, *11*, 488. [\[CrossRef\]](#)
30. Hajian, R.; Soltaninezhad, A. The spectrophotometric multicomponent analysis of a ternary mixture of paracetamol, aspirin, and caffeine by the double divisor-ratio spectra derivative method. *J. Spectrosc.* **2013**, *2013*, 405210. [\[CrossRef\]](#)
31. Nevado, J.J.B.; Cabanillas, C.G.; Salcedo, A.M.C. Spectrophotometric resolution of ternary mixtures of amaranth, carmoisine and ponceau 4R by the derivative ratio spectrum-zero crossing method. *Fresenius J. Anal. Chem.* **1994**, *350*, 606–609. [\[CrossRef\]](#)
32. Morelli, B. Determination of ternary mixtures of antibiotics, by ratio-spectra zero-crossing first- and third-derivative spectrophotometry. *J. Pharm. Biomed. Anal.* **1995**, *13*, 219–227. [\[CrossRef\]](#)
33. Corbella Tena, R.; Rodríguez Delgado, M.A.; Sánchez, M.J.; García Montelongo, F. Comparative study of the ratio spectra derivative and partial least squares methods applied to the simultaneous determination of atrazine and ametryn in ground waters. *Analyst* **1996**, *121*, 459–463. [\[CrossRef\]](#)
34. Piazza, V.; Mazare, A.; Diamanti, M.V.; Peddeferri, M.P.; Schmuki, P. Key oxidation parameters that influence photo-induced properties and applications of anodic titanium oxides. *J. Electrochem. Soc.* **2016**, *163*, H119–H127. [\[CrossRef\]](#)
35. Spurr, R.A.; Myers, H. Quantitative Analysis of anatase-rutile mixtures with an X-ray diffractometer. *Anal. Chem.* **1957**, *29*, 760–762. [\[CrossRef\]](#)
36. IUPAC. Nomenclature, symbols, units and their usage in spectrochemical analysis—III. Analytical flame spectroscopy and associated non-flame procedures. *Pure Appl. Chem.* **1976**, *45*, 105–123. [\[CrossRef\]](#)
37. Kosmulski, M. Isoelectric points and points of zero charge of metal (hydr)oxides: 50 Years after Parks' review. *Adv. Colloid Interface Sci.* **2016**, *238*, 1–61. [\[CrossRef\]](#)
38. Lozano-Álvarez, J.A.; Marañón-Ruiz, V.F.; Jáuregui-Rincón, J.; Medina-Ramírez, I.; Salinas-Gutiérrez, R.; Frausto-Reyes, C. Remoción de colorantes azo con alginato: Relación entre estructura de colorante y eficiencia de remoción. *Rev. Int. Contam. Ambient.* **2019**, *35*, 223–236. [\[CrossRef\]](#)
39. Santos, E.D.B.; Lima, E.C.N.L.; Oliveira, C.S.; De Sigoli, F.A.; Mazali, I.O. Fast detection of paracetamol on a gold nanoparticle-chitosan substrate by SERS. *Anal. Methods* **2014**, *6*, 3564–3568. [\[CrossRef\]](#)
40. Kavitha, C.; Bramhaiah, K.; John, N.S.; Aggarwal, S. Improved surface-enhanced Raman and catalytic activities of reduced graphene oxide–osmium hybrid nano thin films. *R. Soc. Open Sci.* **2017**, *4*, 170353. [\[CrossRef\]](#)
41. Xiao, G.N.; Man, S.Q. Surface-enhanced Raman scattering of methylene blue adsorbed on cap-shaped silver nanoparticles. *Chem. Phys. Lett.* **2007**, *447*, 305–309. [\[CrossRef\]](#)
42. Moreno, V.; Murtada, K.; Zougagh, M.; Ríos, Á. Analytical control of Rhodamine B by SERS using reduced graphene decorated with copper selenide. *Spectrochim. Acta Part A Mol. Biomol. Spectrosc.* **2019**, *223*, 117302. [\[CrossRef\]](#) [\[PubMed\]](#)
43. Lin, S.; Hasi, W.L.J.; Lin, X.; Han, S.Q.G.W.; Lou, X.T.; Yang, F.; Lin, D.Y.; Lu, Z.W. Rapid and sensitive SERS method for determination of Rhodamine B in chili powder with paper-based substrates. *Anal. Methods* **2015**, *7*, 5289–5294. [\[CrossRef\]](#)
44. Ovchinnikov, O.V.; Evtukhova, A.V.; Kondratenko, T.S.; Smirnov, M.S.; Khokhlov, V.Y.; Erina, O.V. Manifestation of intermolecular interactions in FTIR spectra of methylene blue molecules. *Vib. Spectrosc.* **2016**, *86*, 181–189. [\[CrossRef\]](#)
45. Yu, Z.; Chuang, S.S.C. Probing methylene blue photocatalytic degradation by adsorbed ethanol with in situ IR. *J. Phys. Chem. C* **2007**, *111*, 13813–13820. [\[CrossRef\]](#)

46. Baldev, E.; MubarakAli, D.; Ilavarasi, A.; Pandiaraj, D.; Ishack, K.A.S.S.; Thajuddin, N. Degradation of synthetic dye, Rhodamine B to environmentally non-toxic products using microalgae. *Colloids Surf. B Biointerfaces* **2013**, *105*, 207–214. [[CrossRef](#)] [[PubMed](#)]
47. Mchedlov-Petrosyan, N.O.; Fedorov, L.A.; Sokolovskii, S.A.; Surov, Y.N.; Maiorga, R.S. Structural conversions of rhodamines in solution. *Bull. Russ. Acad. Sci. Div. Chem. Sci.* **1992**, *41*, 403–409. [[CrossRef](#)]
48. Li, J.; Ma, W.; Lei, P.; Zhao, J. Detection of intermediates in the TiO₂-assisted photodegradation of Rhodamine B under visible light irradiation. *J. Environ. Sci.* **2007**, *19*, 892–896. [[CrossRef](#)]
49. Farag, A.A.M.; Yahia, I.S. Structural, absorption and optical dispersion characteristics of Rhodamine B thin films prepared by drop casting technique. *Opt. Commun.* **2010**, *283*, 4310–4317. [[CrossRef](#)]
50. Dukali, R.M.; Radovic, I.M.; Stojanovic, D.B.; Sevic, D.M.; Radojevic, V.J.; Jovic, D.M.; Aleksic, R.R. Electrospinning of the laser dye rhodamine B-doped poly(methyl methacrylate) nanofibers. *J. Serb. Chem. Soc.* **2014**, *79*, 867–880. [[CrossRef](#)]
51. Madami, W.; Seoudi, R. Molecular and fluorescence spectroscopic studies of polyacrylic acid blended with rhodamine B mixed gold nanoparticles. *J. Taibah Univ. Sci.* **2020**, *14*, 790–799. [[CrossRef](#)]
52. Carroll, M.K.; Unger, M.A.; Leach, A.M.; Morris, M.J.; Ingersoll, C.M.; Bright, F.V. Interactions between methylene blue and sodium dodecyl sulfate in aqueous solution studied by molecular spectroscopy. *Appl. Spectrosc.* **1999**, *53*, 780–784. [[CrossRef](#)]
53. Mahmoodi, N.M.; Arami, M.; Limaee, N.Y.; Tabrizi, N.S. Decolorization and aromatic ring degradation kinetics of Direct Red 80 by UV oxidation in the presence of hydrogen peroxide utilizing TiO₂ as a photocatalyst. *Chem. Eng. J.* **2005**, *112*, 191–196. [[CrossRef](#)]
54. Lin, J.; Luo, Z.; Liu, J.; Li, P. Photocatalytic degradation of methylene blue in aqueous solution by using ZnO–SnO₂ nanocomposites. *Mater. Sci. Semicond. Process.* **2018**, *87*, 24–31. [[CrossRef](#)]
55. Yu, K.; Yang, S.; He, H.; Sun, C.; Gu, C.; Ju, Y. Visible light-driven photocatalytic degradation of Rhodamine B over NaBiO₃: Pathways and mechanism. *J. Phys. Chem. A* **2009**, *113*, 10024–10032. [[CrossRef](#)]
56. Byberg, R.; Cobb, J.; Martin, L.D.; Thompson, R.W.; Camesano, T.A.; Zahraa, O.; Pons, M.N. Comparison of photocatalytic degradation of dyes in relation to their structure. *Environ. Sci. Pollut. Res.* **2013**, *20*, 3570–3581. [[CrossRef](#)] [[PubMed](#)]
57. Muthukumar, M.; Sargunamani, D.; Selvakumar, N. Statistical analysis of the effect of aromatic, azo and sulphonic acid groups on decolouration of acid dye effluents using advanced oxidation processes. *Dye. Pigment.* **2005**, *65*, 151–158. [[CrossRef](#)]
58. Konstantinou, I.K.; Albanis, T.A. TiO₂-assisted photocatalytic degradation of azo dyes in aqueous solution: Kinetic and mechanistic investigations: A review. *Appl. Catal. B Environ.* **2004**, *49*, 1–14. [[CrossRef](#)]
59. Gomathi Devi, L.; Narasimha Murthy, B.; Girish Kumar, S. Heterogeneous photo catalytic degradation of anionic and cationic dyes over TiO₂ and TiO₂ doped with Mo⁶⁺ ions under solar light: Correlation of dye structure and its adsorptive tendency on the degradation rate. *Chemosphere* **2009**, *76*, 1163–1166. [[CrossRef](#)]
60. Miran, W.; Rasool, K.; Nawaz, M.; Kadam, A.; Shin, S.; Heo, J.; Jang, J.; Sung Lee, D. Simultaneous electricity production and Direct Red 80 degradation using a dual chamber microbial fuel cell. *Desalin. Water Treat.* **2016**, *57*, 9051–9059. [[CrossRef](#)]
61. Lops, C.; Ancona, A.; Di Cesare, K.; Dumontel, B.; Garino, N.; Canavese, G.; Hernández, S.; Cauda, V. Sonophotocatalytic degradation mechanisms of Rhodamine B dye via radicals generation by micro- and nano-particles of ZnO. *Appl. Catal. B Environ.* **2019**, *243*, 629–640. [[CrossRef](#)]

